**Biogeosciences
Discussions**

# Controls on the spatial distribution of oceanic $\delta^{13}C_{DIC}$

P. B. Holden[1], N. R. Edwards[1], S. A. Müller[2], K. I. C. Oliver[2], R. M. Death[3], and A. Ridgwell[3]

[1]Environment, Earth and Ecosystems, Open University, Milton Keynes, UK
[2]Ocean and Earth Science, National Oceanography Centre Southampton, University of Southampton, Southampton, UK
[3]School of Geographical Sciences, University of Bristol, Bristol, UK

Correspondence to: P. B. Holden (p.b.holden@open.ac.uk)

Title Page

Abstract | Introduction

Conclusions | References

Tables | Figures

|◄ | ►|

◄ | ►

Back | Close

Full Screen / Esc

Printer-friendly Version

Interactive Discussion

**Controls on the spatial distribution of oceanic $\delta^{13}C_{DIC}$**

P. B. Holden et al.

## Abstract

We describe the design and evaluation of a large ensemble of coupled climate-carbon cycle simulations with the Earth-system model of intermediate complexity GENIE. This ensemble has been designed for application to a range of carbon cycle questions including utilizing carbon isotope ($\delta^{13}C$) proxy records to help constrain the state at the last glacial. Here we evaluate the ensemble by applying it to a transient experiment over the recent industrial era (1858 to 2008 AD). We employ singular vector decomposition and principal component emulation to investigate the spatial modes of ensemble-variability of oceanic dissolved inorganic carbon (DIC) $\delta^{13}C$, considering both the spun-up pre-industrial state and the transient change due to the $^{13}C$ Suess Effect. These analyses allow us to separate the natural and anthropogenic controls on the $\delta^{13}C_{DIC}$ distribution. We apply the same dimensionally reduced emulation techniques to consider the drivers of the spatial uncertainty in anthropogenic DIC. We show that the sources of uncertainty governing the uptake of anthropogenic $\delta^{13}C_{DIC}$ and DIC are quite distinct. Uncertainty in anthropogenic $\delta^{13}C$ uptake is dominated by uncertainties in air-sea gas exchange, which explains 63 % of modelled variance. This mode of variability is absent from the ensemble variability in $CO_2$ uptake, which is rather driven by uncertainties in ocean parameters that control mixing of intermediate and surface waters. Although the need to account for air-sea gas exchange is well known, these results suggest that, to leading order, uncertainties in the $^{13}C$ Suess effect and anthropogenic $CO_2$ ocean-uptake are governed by different processes. This illustrates the difficulties in reconstructing one from the other and furthermore highlights the need for improved spatial coverage of both $\delta^{13}C_{DIC}$ and DIC observations to better constrain the ocean sink of anthropogenic $CO_2$.

# 1 Introduction

A substantial component of the uncertainty associated with both anthropogenic and natural climate change derives from uncertainties in the carbon cycle. The natural climate variability over the last 800 000 yr, driven by orbital changes of the Earth about the Sun, have been associated with changes in atmospheric $CO_2$ with amplitudes of $\sim 90$ ppm (Lüthi et al., 2008). Numerous hypotheses have been proposed to explain this variability, but their relative contributions are still poorly understood (Kohfeld and Ridgwell, 2009). Improved understanding is also required to better quantify the response of the Earth System and changing strength of various feedbacks to ongoing carbon emissions, especially given recent observations that the oceanic carbon sink is weakening (Le Quéré et al., 2007). For instance, while coupled climate-carbon cycle models consistently predict a weakened efficiency of the ocean-terrestrial carbon sink under future emissions scenarios, they do so with a highly uncertain magnitude with predictions of year 2100 atmospheric $CO_2$ ranging from 740 to 1030 ppm (Friedlingstein et al., 2006). Entraining observations in addition to that of atmospheric $CO_2$ is essential to better constrain such carbon cycle changes.

Anthropogenic emissions of $CO_2$ from the burning of fossil fuels and deforestation are strongly depleted in $^{13}C$, reflecting the preferential uptake of $^{12}C$ during photosynthesis. As a consequence, the $\delta^{13}C$ composition of the atmosphere, where $\delta^{13}C = 1000((^{13}C/^{12}C)_{sample}/(^{13}C/^{12}C)_{standard} - 1)$, has decreased from about $-6.5$‰ in pre-industrial times to $-8.2$‰ in the present day (Keeling et al., 2010). It has also produced an imprint on the oceanic $\delta^{13}C_{DIC}$ distribution (Gruber et al., 1999), known as the $^{13}C$ Suess Effect (Keeling, 1979), which can then be employed to help constrain estimates of fossil fuel emissions and their uptake (e.g. Joos and Bruno, 1998; Quay et al., 2003). However, the oceanic $\delta^{13}C$ distribution reflects a complex interplay between marine productivity, water column remineralization of organic matter, ocean circulation and mixing, and air-sea gas exchange (Gruber et al., 1999; Tagliabue and Bopp, 2008). A clear understanding of the factors that control the distribution of the

$^{13}$C/$^{12}$C ratio in the ocean is essential if observations of $\delta^{13}C_{DIC}$ are to be of use in constraining either modern or glacial carbon cycling.

Faced with large uncertainties in multiple processes and feedbacks in the global carbon cycle, Earth System Models of Intermediate Complexity (EMICs) have become important tools for helping explore process sensitivities and quantifying uncertainty. Carefully designed ensembles of simulations can be used to derive data-constrained probability distributions and complement high-complexity (but small in number) simulations of fully coupled ocean-atmosphere based Earth system models. We take this approach here, describing an ensemble of instances of an EMIC and associated analysis of the controls on anthropogenic $CO_2$ and $\delta^{13}C$ uptake by the ocean.

In this paper: Sects. 2 to 5 describe the development and evaluation of a perturbed-parameter ensemble of the Grid Enabled INtegrated Earth system model (GENIE). This ensemble has been applied to several transient historical and future carbon-cycle experiments (Eby et al., 2012; Holden et al., 2012; Joos et al., 2012; Zickfeld et al., 2012). However, its underlying experimental design and choice of variable parameters is governed by consideration of the processes that are thought to contribute to variability of atmospheric $CO_2$ on glacial-interglacial timescales, as summarised in Kohfeld and Ridgwell (2009). The motivation for this approach is: (a) to create the flexibility for carrying out glacial-interglacial experiments and (b) by assuming that the processes important in setting glacial $CO_2$ include those which govern the distributions of carbon and carbon isotopes in the modern ocean, enable rigorous evaluation against modern observations and other models. Sections 6 and 7 then describe the application of this ensemble to investigate the processes controlling the $\delta^{13}C_{DIC}$ distribution in both the pre-industrial (assumed equilibrium) ocean state and transient industrial change due to the Suess effect. In both cases we apply singular vector decomposition to identify the spatial patterns corresponding to the dominant modes of variability amongst the simulations. Emulation of the principal components, following Holden and Edwards (2010), then enables us to evaluate the processes and parameters driving this simulated variability. We further apply this analytical approach to the oceanic uptake of

**Controls on the spatial distribution of oceanic $\delta^{13}C_{DIC}$**

P. B. Holden et al.

Full Screen / Esc

Printer-friendly Version

Interactive Discussion

anthropogenic $CO_2$ in order to examine the relationship between the resulting changes to oceanic distributions of DIC and $\delta^{13}C_{DIC}$.

## 2 The GENIE configuration

We utilize a coupled carbon cycle-climate configuration of GENIE (version 2.7.7). The physical model comprises the 3-D frictional geostrophic ocean model GOLDSTEIN (at $36 \times 36 \times 16$ resolution) coupled to a 2-D Energy Moisture Balance model of the atmosphere (EMBM) and a thermodynamic-dynamic sea-ice model (Edwards and Marsh, 2005; Marsh et al., 2011). Adjustments to the parameterisations of outgoing long wave radiation (OLR) and lapse rate effects are described in Holden et al. (2010). Notable recent refinements to the ocean model are the addition of stratification dependent mixing (Oliver and Edwards, 2008), the inclusion of the thermobaricity term in the equation of state (Oliver, 2012) and the incorporation of alternative wind forcing fields which have improved the representation of global ocean circulation, especially in terms of the strength of the Antarctic Circumpolar Current (Marsh et al., 2011). The land surface module is the model of terrestrial carbon storage ENTS (Williamson et al., 2006). Ocean biogeochemistry is modelled with BIOGEM, based on the model of Ridgwell et al. (2007a), including the cycling of iron described by Annan and Hargreaves (2010) except with biological uptake following Doney et al. (2006). For consistency with the wind stress forcing of the ocean model, the prescribed wind speed field used by Ridgwell et al. (2007a) to compute the squared-wind speed coefficient in the air-sea gas exchange parameterisation was replaced with wind speeds derived from the annual-mean wind-stress climatology applied in the ocean model component. Sediments are modelled with SEDGEM at $36 \times 36$ resolution as per Ridgwell and Hargreaves (2007). The rock-weathering module ROKGEM (Colbourn, 2011) is included to redistribute prescribed weathering fluxes according to a fixed river-routing scheme.

For each ensemble member (see Sect. 3), the model was first spun up for 25 000 yr in order to bring the sediments close to equilibrium with pre-industrial boundary

conditions. Atmospheric $CO_2$ and $\delta^{13}C$ were relaxed to pre-industrial values of 278 ppm and −6.5‰, respectively. During model spin-up, ocean biogeochemistry was simulated as a closed system (i.e. sedimentary fluxes, except iron, were returned at the bottom of the ocean) and weathering fluxes required to balance sediment burial were diagnosed at the end of the spin-up phase (Ridgwell and Hargreaves, 2007). In order to perform the industrial transient simulations (1858 to 2008 AD), the sediment system was opened (i.e. exchanges of sediment-ocean fluxes were applied as simulated by the sediment model), applying the constant weathering flux. Atmospheric $CO_2$ and $\delta^{13}C$ were relaxed to temporally prescribed observations.

## 3   Ensemble design

The philosophy for the design process has been described in detail elsewhere (Holden et al., 2010). In short, the approach attempts to vary key model parameters over the entire range of plausible input values and to accept parameter combinations which lead to climate states that cannot be un-controversially ruled out as implausible (Edwards et al., 2011). The approach represents an attempt to find plausible realisations of the model from all regions of the high-dimensional input parameter space in order to capture the range of possible feedback strengths.

## 3.1 Parameters

We varied 24 model parameters in the ensemble[1] (see Table 1). Overall, the model configuration and choice of variable parameters was governed by consideration of the processes that are thought to contribute to variability of atmospheric $CO_2$ on glacial-interglacial timescales (Kohfeld and Ridgwell, 2009) and hence to which the distributions of carbon and carbon isotopes may be potentially sensitive in general. These processes are summarised as follows:

**Ocean circulation**

The frictional parameter of the ocean model (ODC) and three ocean diffusivity parameters (OHD, OVD and OP1) are varied. The uncertain impact of winds on stratification is captured through the wind stress scaling parameter (WSF). The parameters having the strongest impact on the physical climate were chosen as those that control global temperature, Atlantic overturning strength, Antarctic sea-ice coverage and terrestrial carbon inventories, as identified from previous ensembles (Fig. 2 of Holden et al., 2010). By varying sea-ice diffusivity (SID) we attempt to represent uncertainty introduced by brine rejection on AABW. Brine rejection is a potential mechanism for increasing deep ocean stratification and drawing down $CO_2$ from the atmosphere in the glacial state (Bouttes et al., 2010). Bouttes et al. (2011), in the 2-D CLIMBER-2 ocean model find that GIG changes in $CO_2$ and $\delta^{13}C$ gradients can be simultaneously reconciled with judicious combinations of enhanced brine-rejection driving southern deep-water formation, stratification-dependent mixing, and iron fertilisation, all playing substantial roles.

---

[1] An additional, dummy parameter (PMX), was included in error. The basic configuration of the biogeochemical model was changed late in the design process to incorporate the most up-to-date iron-cycling scheme. Instead of a parameter for the maximum phosphate uptake (PMX), the iron-cycling scheme prescribes a phosphate uptake timescale but the configuration files were not updated to reflect this. The effect of not varying the phosphate uptake will be discussed below.

Full Screen / Esc

Printer-friendly Version

Interactive Discussion

Varying SID across these wide ranges provides a means to vary this feedback strength in a way that naturally connects the dynamics of brine rejection and sea-ice. A wide range of Atlantic circulation states, ranging from the near-total dominance of AABW to the total dominance of NADW can be achieved by spanning the ranges for SID in Table 1. Whilst it is difficult to quantify the plausible range of input space, we rather choose an input range that spans the not-implausible range of output space and then constrain output space accordingly. We note that the SID range considered here extends to substantially higher values than have been considered in previous ensembles (e.g. Edwards and Marsh, 2005; Holden et al., 2010; Edwards et al., 2011).

## $CO_2$ solubility and sea surface temperature

$CO_2$ is more soluble in cold water, leading to drawdown of atmospheric $CO_2$ in the glacial state in comparison to the modern state. The wide range of ensemble climate states, including a wide spread of equator-to-pole temperature gradients (Holden et al., 2010) across the ensemble captures the uncertainty arising from this effect.

## Iron Fertilization

Increased glacial dust fluxes are thought to have more-strongly fertilized the iron-limited regions such as the Southern Ocean, increasing productivity and thus potentially providing a mechanism for additional $CO_2$ drawdown in the glacial state (Watson et al., 2000). Iron supply to the ocean is included, and varied, in the experiment by prescribing the pre-industrial dust fluxes of Mahowald et al. (2005) and varying the soluble iron fraction.

### Rain ratio

Oceanic biological activity affects atmospheric $CO_2$ concentrations through changes in the relative rates of $CaCO_3$ and Particulate Organic Carbon (POC) supply to the seafloor. Uncertainty is captured through parameters controlling the export ratio and

remineralisation depths. Changes in Redfield ratios or remineralisation depths have the potential to cause significant changes in carbon isotope and DIC storage and may be linked to climate (Omta et al., 2006). While the dynamics of possible feedbacks may not be captured, the wide range of input values allows us to capture possible sensitivity to these processes.

## Carbonate compensation

When the distribution of oceanic dissolved carbon and/or alkalinity is changed, the stability of $CaCO_3$ in the sediments responds. No sediment parameters were varied in this study, but a wide range of sediment states (Sect. 3.2) is allowed in order to capture the uncertainty in this feedback.

## Air-sea gas exchange

Air-sea gas exchange rates exert controls on the degree of ocean-atmosphere equilibration and ^{13}C fractionation. The globally uniform coefficient of the air-sea gas exchange parameterisation (ASG) was varied in the ensemble design.

## Sea-ice cover

A change in sea-ice extent can modify the rate of air-sea gas exchange in polar oceans. Chikamoto et al. (2012) find that although increased sea-ice cover in the Antarctic can reduce outgassing of $CO_2$, as predicted by Stephens and Keeling (2000), this can be offset by reduced uptake as a result of increased sea-ice cover in northern deep-water formation regions. A wide range of sea-ice coverage was allowed in the ensemble (Sect. 3.2).

### Terrestrial carbon

Uncertainty in terrestrial vegetation is captured through five key parameters of the terrestrial vegetation model (VFC, VBP, VRA, LLR and SRT). We note that in the experiments described here, vegetation uncertainty is only relevant through its direct impact on climate (by way of changes in albedo, surface roughness and soil moisture storage) as atmospheric concentrations of $CO_2$ and carbon isotopes are relaxed to observational estimates. The vegetation parameters were varied in anticipation of future experiments with freely-evolving $CO_2$.

### 3.2 Statistical design

An investigative ensemble was performed with a 500-member Maximin Latin Hypercube (MLH) design for 26 parameters. The 26th parameter was included as a dummy parameter but was not required in this analysis as PMX serves to fulfil this role (Sect. 3.1). A regression-based predictor, including linear and quadratic terms, was built for each of eight metrics from the output of the MLH ensemble (Holden et al., 2010). The eight metrics were chosen to provide global-scale constraints on atmosphere, ocean (NADW and Atlantic AABW), Antarctic sea ice coverage, terrestrial carbon (vegetation and soil), ocean biogeochemistry and ocean sediments. The metrics are summarised in Table 2. Parameters were then sampled randomly from a uniform distribution between plausible ranges (Table 1) and applied as input to these emulators. A parameter set was accepted as potentially plausible when the emulators predicted values within the "Approximate Bayesian Calibration" (ABC) ranges in Table 2 for all eight metrics. The ABC filtering ranges are centred on observations. They are reduced relative to the plausibility ranges in order to more efficiently generate plausible simulations (i.e. acknowledging that the emulations are imperfect) with a reduction chosen cognisant of the individual emulator errors. Note the poorly centred ABC range for Antarctic sea ice. The range was selected based on estimates of annually-averaged area ($\sim 10$ million km$^2$) but was applied to an emulation of 31 December coverage (esti-

mated to be $\sim 7$ million km$^2$, Cavalieri et al., 2003). Given the similarity of these metrics (given the wide range accepted as plausible and the emulator error) this did not result in a bias to the ensemble (see Table 2), although it did result in a $\sim 15\%$ increase in the emulator failure rate.

5     Each emulator-filtered parameter set was then applied as input to a further simulation. As simulations completed, the emulators were rebuilt four times including the additionally available data. This process progressively improved the success rate of the ABC selection from 24% to 65%. In total, 1000 emulator-filtered parameter sets were applied to the simulator. These produced 885 completed simulations of which 10  471 were plausible. This 471-member subset forms the Emulator Filtered Plausibility Constrained (EFPC) ensemble.

## 4   Plausibility emulators and total effects

It is useful to apply the plausibility emulators (Sect. 3.2) in order to investigate the role played by the parameters values in determining the spun-up state, the principal 15  motivation being to inform future ensemble design. To achieve this, we calculate the "total effect" (Saltelli et al., 2000) of each parameter in each of the emulators. The total effect of a parameter is equal to the expectation of the variance that remains when we have learnt everything about the model besides the value of that parameter. See Holden et al. (2010) for a more complete description of the method. Figure 1 illustrates 20  the total effects for each of the eight plausibility emulators. For each emulator, the total effect is normalised to total 100%, thus illustrating the relative importance for each parameter in determining the plausible modern state (as defined by the acceptable input ranges in Table 1 and output ranges in Table 2).

    This analysis was previously performed on the SAT, MAXA, SHSI, CVEG and CSOIL 25  emulators and is discussed in some detail in Holden et al. (2010). Three parameters (AMD, OL0 and VFC) appear less important in this revised analysis. However, this likely reflects the fact that the ranges for these parameters were narrowed for this en-

P. B. Holden et al.

semble (by 40 %, 25 % and 23 %, respectively), highlighting that total effects are not purely objective measures as they are dependent upon estimates of the ranges of input parameters. We note further that MAXA emulator is intrinsically different given the refinements to the ocean model applied in this study (Sect. 2).

In addition to the tests used by Holden et al. (2010), a test for minimum Atlantic overturning strength was introduced to enforce the constraint that plausible ensemble members have an overturning cell associated with AABW. As with all eight plausibility filters, no constraint was imposed upon its spatial distribution, just the maximum value of the stream function (at depths below 500 m and latitudes north of 30° S). The strength of the AABW cell is controlled by atmospheric moisture transport, isopycnal diffusivity, ocean drag and sea-ice diffusivity, each of which play comparably important roles. It is notable that high values of the SID parameter are not necessary to generate a strong AABW cell: for instance, low values of isopycnal diffusivity seem to achieve this objective equally efficiently. However, when several parameters are capable of achieving a similar result independently, it is useful to vary them all in order to span as much plausible input space as is possible. Moreover, the primary reason for including SID as a variable parameter in the ensemble was to span a range of circulation feedback strengths in response to changing sea-ice coverage.

The percentage of $CaCO_3$ in the surface sediment is unsurprisingly controlled by the parameters that control the export of $CaCO_3$, i.e. the 2 parameters (RRS, TCP) controlling the $CaCO_3$ : POC rain ratio at every grid point (see: Ridgwell et al., 2007a,b) and the fraction of exported $CaCO_3$ assumed to reach the sediment surface without being subject to water column dissolution (PRC). Also apparent is the importance of parameters controlling the flux of organic mater to the sediments (PRP, PRD) and thereby promoting $CaCO_3$ dissolution. Dissolved oxygen is mainly controlled by circulation strength and mixing (through APM, OVD, OP1, ODC, WSF), presumably through their role in redistributing nutrients (and oxygen) within the ocean, the POC remineralisation depth (PRD, via its control on respiration in the deep ocean) and iron solubility (FES) which exerts a strong control on productivity. The phosphate half-saturation

concentration (PHS) does not appear as a strong control, suggesting that uncertainty in productivity is not dominated by the rate of phosphate uptake, but rather the rate of phosphate redistribution. The dominance of parameters that control the supply of phosphate, rather than the rate of phosphate uptake, suggest that the omission of the maximum rate of phosphate uptake has not resulted in a substantial underestimation of the uncertainty associated with phosphate limitation. In contrast, iron solubility does play a significant role through its influence in determining the extent of iron-limited regions.

## 5  Ensemble evaluation

The ensemble design intentionally avoids tuning the model in the conventional sense. The philosophy reflects the acceptance of the fact that, on account of the unknown dynamic behaviour of structural errors that are inevitable in any model, the simulation that best predicts unobserved variables or future change is not necessarily that which most closely fits observations. Consequently, the evaluation performed here is intended to demonstrate the degree to which the eight plausibility constraints are sufficient to produce simulations that we would not rule out as uncontroversially implausible, and to identify biases or structural errors in the ensemble-averaged spatial distributions.

Figure 2 plots Taylor diagrams for the model-data comparison between the EFPC ensemble and observation fields for four oceanic properties: dissolved phosphate, dissolved oxygen, temperature and salinity. The diagrams depict the relative performance of the 471 ensemble members as well as the outputs of an optimised biogeochemical configuration (Ridgwell and Death, 2012) for comparison. Figures 3 and 4 illustrate surface fields and latitude-depth transects through the Atlantic (25° W) for the same properties, in each case comparing observations with EFPC ensemble averages. Observed surface fields are depth-averages over the vertical extent of the surface layer of the ocean model, approximately 81 m.

## 5.1 Dissolved phosphate

The ensemble-averaged correlation of dissolved phosphate with respect to observations (Garcia et al., 2006) is +0.88, compared to the optimised model correlation of +0.91. The ensemble-averaged variability of the spatial distribution captures the variability of the observations more closely than the optimised model (the cloud is approximately centred on a normalised standard deviation of 1). These statistics together suggest that the neglect of the maximum phosphate uptake as a variable parameter has not biased the ability of the ensemble to capture a wide range of phosphate distributions that are consistent with observations. The ensemble-averaged surface field of dissolved phosphate compares reasonably with observations, although the increased concentrations associated with upwelling regions are not well captured so that phosphate is near-fully utilised throughout low and mid latitude oceans. Only 20 simulations exhibit surface-layer averaged phosphate concentrations that exceed observation estimates of $0.6\,\mu mol\,kg^{-1}$. The Atlantic cross-section compares favourably with observations, although the volume and northerly extent of AABW are overestimated in the ensemble average. This may be a consequence of the very high sea-ice diffusivities (SID) that have been allowed in the ensemble leading to increased brine rejection and AABW production. The EFPC distribution for SID is $52\,000 +/- 26\,000\,m^2\,s^{-1}$ ($1\sigma$ uncertainties are quoted throughout). Previous studies that have generally not considered values above $25\,000\,m^2\,s^{-1}$ (e.g. Edwards et al., 2011).

## 5.2 Dissolved oxygen

Dissolved oxygen exhibits an ensemble-averaged correlation of +0.76 (c.f. +0.83 in the optimised model) and the normalised standard deviation is approximately centred on unity, demonstrating a comparable spatial variability to observations (Garcia et. al., 2006). The major weakness of the surface distribution reflects the weaknesses of the phosphate distributions; oxygen depleted regions associated with equatorial upwelling are not captured by the model. The dissolved oxygen cross-section compares well

to observations, a conspicuous difference being a ~20 % underestimate of oxygen in NADW which, in the absence of large differences in temperature (Sect. 5.3 below), is suggestive of excess productivity in high northern latitudes and consistent with the underestimate of surface phosphate in the Arctic (Fig. 3). It could also reflect a bias towards low rates of air-sea gas exchange (see: Sect. 7), preventing the N. Atlantic surface from fully equilibrating with the atmosphere. The plausibility constraints require reasonable globally averaged oxygen concentrations (~170 µmol kg$^{-1}$). It appears that the underestimate of equatorial productivity, which we interpret as caused by a structural issue, which cannot be addressed through the varied parameters, may have been compensated for by favouring parameters that compensate by increasing productivity in high latitudes, notably high northern latitudes that are not Fe-limited.

## 5.3 Temperature

Temperature exhibits an ensemble-averaged correlation with observations (Locarnini et al., 2006) of +0.96, comparable to the optimised model. The spatial variability tends to be greater than observations, a feature which is shared with the optimised model. The ensemble-averaged SST field agrees very well with observations, so that the overestimate of spatial variability is not reflected in this layer. The ensemble-averaged equator-to-pole SST temperature gradient reflects observations closely, important here given the strong temperature dependence of carbon isotope fractionation during air-sea gas exchange (Mook, 1986). The overestimate of the spatial variance is rather related to the vertical temperature gradient (Fig. 4), which is greater than observations. This is likely, at least in part, a further consequence of the excessive strength of the AABW cell in the ensemble average.

## 5.4 Salinity

The ensemble-averaged salinity correlation with observations (Antonov et al., 2006) is +0.44 (c.f. +0.77 in the optimised model). Poor salinity correlations are expected

as atmospheric moisture transport in the simple EMBM is dominated by diffusion. In the Bern3D model (structurally very similar to the configuration of GENIE used here as both are based on the same progenitor ocean model), optimised salinity correlations of 0.65 were obtained (Ritz et al., 2011), compared to 0.9 when the ocean
5  model was restored to climatological sea-surface temperature and salinity fields (Müller et al., 2006). The salinity correlation across the EPFC ensemble (i.e. the correlation displayed separately by each of the 471 simulated fields with observations) exhibits a correlation of 0.54 with the atmospheric moisture diffusivity parameter (AMD). Low atmospheric diffusivity inhibits moisture transport out of low latitudes, restricting the de-
10  velopment of the increased surface salinities that are observed there. EPFC-averaged AMD of $8.4 \times 10^5 \, \text{m}^2 \, \text{s}^{-1}$ is somewhat low compared to optimised values ranging between $\sim 1 \times 10^6$ and $3 \times 10^6 \, \text{m}^2 \, \text{s}^{-1}$ (Lenton et al., 2006). We note that the sign of the vertical salinity gradient in the Pacific can be reversed due to this effect resulting in the very low correlations that are seen in some ensemble members.
15  An important decision therefore was whether to apply additional filters to the EPFC ensemble in order to eliminate those simulations with poorly correlated salinity fields. Outside of the Arctic, the spatial pattern of the ensemble mean surface salinity is reasonable, although it exhibits a bias of $\sim -1$ psu (Fig. 3). We note that the ensemble variability of Atlantic (Pacific) surface salinity varies spatially from $\sim 0.2$ to 0.4 psu ($\sim 0.5$
20  to 1 psu). The salinity latitude-depth cross-sections in the Atlantic compare reasonably with observations (Fig. 4), though again they exhibit a low bias. The major disagreement is thus the understated surface salinities at low to mid latitudes, which may have important consequences for biological production via impacts on stratification-dependent mixing and the redistribution of nutrients back to the photic zone. To test for
25  this, a salinity-correlation filter was applied to leave only the 112 ensemble members with a salinity correlation > 0.6. The cross-sections of 112-member ensemble-averaged phosphate, oxygen and $\delta^{13}\text{C}_{\text{DIC}}$ in the Atlantic, Pacific and Indian oceans were very similar those of the complete EFPC ensemble, suggesting that the impact of the freshened surface waters on biological production is not significant, especially given the

Title Page

Abstract | Introduction

Conclusions | References

Tables | Figures

|◄ | ►|

◄ | ►

Back | Close

Full Screen / Esc

Printer-friendly Version

Interactive Discussion

philosophy of the ensemble design. To illustrate, a comparison of the $\delta^{13}C_{DIC}$ cross-sections of the means of the two ensembles exhibits an $R^2$ of $> 99\%$ in all three basins, although the salinity-filtered ensemble exhibits a slightly elevated average $\delta^{13}C_{DIC}$ (0.89 ‰ c.f. 0.85 ‰ in the Atlantic, 0.40 ‰ c.f. 0.23 ‰ in the Pacific and 0.61 ‰ c.f. 0.55 ‰ in the Indian Oceans). We decided to retain all 471 of the EFPC members, anticipating that the benefits of a large ensemble likely outweigh any beneficial effects of applying this filter.

## 5.5 Ocean $\delta^{13}C_{DIC}$

Figure 5 shows EPFC pre-industrial and modern (2008 AD) ensemble-averaged latitude-depth transects of $\delta^{13}C_{DIC}$ through the Atlantic (25° W) and Pacific (155° W). The discussion in the following paragraphs addresses the evaluation of the simulated present day $\delta^{13}C_{DIC}$ distribution with respect to the observational data of Kroopnick (1985, Figs. 3 and 5 therein) and Gruber et al. (1999).

In the Atlantic, ensemble-averaged $\delta^{13}C_{DIC}$ of AABW and AAIW masses varies in the range $\sim 0.3$ ‰ to $\sim 0.7$ ‰ and NADW varies in the range $\sim 0.7$ ‰ to $\sim 1.2$ ‰, in both cases consistent with observations (Kroopnick, 1985). The simulated 0.75 ‰ contour extends to $\sim 35°$ S, again in good agreement with the observational data, but only reaches depths of $\sim 3000$ m, in disagreement with the observations, which indicate that values in excess of 0.7 ‰ extend to the ocean floor north of the Equator. This is consistent with the excessive northerly penetration of AABW that is apparent in the phosphate distribution (Sect. 5.1). We note that ensemble-averaged oceanic-mean $\delta^{13}C_{DIC} = 0.38 +/-0.22$ ‰ is slightly lower than observational estimates of 0.5 ‰ (Quay et al., 2003), also consistent with too much simulated AABW.

In the Pacific, ensemble averaged $\delta^{13}C_{DIC}$ at depths below 1000 m ranges from $\sim -0.5$ ‰ at high northern latitudes to $\sim 0.4$ ‰ at high southern latitudes. These are in reasonable agreement with observations, although observational data reaches values

as low as −1.0‰ at high northern latitudes. In the simulations, the 0‰ contour extends south to ∼ 10° S and to depths of ∼ 3000 m, in good agreement with observations.

Simulated surface values of $\delta^{13}C_{DIC}$ in the Pacific of ∼ 1.5‰ are ∼ 0.3‰ lower than observations of Gruber et al. (1999), consistent with a $^{13}C$ Suess effect of −0.018‰ yr$^{-1}$ (Gruber et al., 1999). Simulated Atlantic surface $\delta^{13}C_{DIC}$ of ∼ 2‰ is comparable to Gruber et al. (1999), so that the lack of a "Suess-offset" indicates a high-bias (∼ 0.3‰) in simulations of surface Atlantic $\delta^{13}C_{DIC}$. Meridional surface profiles display similar characteristics to observations of Gruber et al. (1999): low values (∼ 1‰) at high southern latitudes of the Atlantic, a maximum in both basins at ∼ 40° S to 50° S, a peak in the Pacific at ∼ 15° S and a trough in the Atlantic at ∼ 30° N (located at ∼ 20° N in the simulations). These complex surface distributions can be explained through the interplay of the temperature-dependent fractionation of air-sea exchange, upwelling of $^{13}C$ depleted waters in the Southern Ocean and meridionally variable biological uptake rates and fractionation, greatest in regions of nutrient upwelling and lowest in the centres of sub-tropical gyres (Gruber et al., 1999).

# 6  Drivers of the spatial distribution of pre-industrial $\delta^{13}C_{DIC}$

Aside from the excessive northerly intrusion of AABW and the ∼ 0.3‰ high-bias in surface Atlantic $\delta^{13}C_{DIC}$, the ensemble-averaged $\delta^{13}C_{DIC}$ spatial distributions are in good agreement with the observations of Kroopnick (1985) and Gruber et al. (1999). The following analysis seeks to explain the processes and parameters that determine the spatial distributions. We apply singular vector decomposition (SVD) to determine the dominant patterns (empirical orthogonal functions, EOFs) of variability across the ensemble and then to emulate the principal components (PCs) as functions of model parameters. Any of the simulated fields can be constructed as a linear combination of EOFs, weighted by their respective PCs. As such, an emulation of a PC can be used to quantify the contribution of each parameter to the uncertainty associated with the respective EOF. We analyse both the pre-industrial spun-up states and the transient

anomaly (the difference between years 2008 and 1858) in order to separate equilibrium effects from the $^{13}$C Suess effect.

## 6.1 EOF decomposition

We consider two latitude-depth transects through the Atlantic (25° W) and Pacific (155° W). These transects run between latitudes 71° S and 63° N, thus including the Southern Ocean but not the Arctic Ocean. The EFPC ensemble was decomposed into EOFs by applying SVD to the centred fields (i.e. after subtracting the ensemble mean). The SVD was applied to a single column vector constructed from the combined Atlantic and Pacific fields in order to derive a single set of EOFs that consistently describes both basins. Figure 6 shows the first three EOFs, plotted separately in the two basins. These three EOFs explain 42 %, 27 % and 11 % of the variance across the ensemble. Figure 6 additionally shows the emulator coefficients associated with each EOF, discussed in Sect. 6.2.

The first EOF is of the same sign (negative) at every location across the two basins, suggesting that this EOF relates primarily to a global-scale change in oceanic $\delta^{13}C_{DIC}$. This change is not uniformly distributed throughout the global ocean, but is qualitatively similar to the spatial pattern of the ensemble mean in both basins (Fig. 5). The correlation between globally averaged $\delta^{13}C_{DIC}$ and the 1st PC is −0.93, confirming this interpretation. (Note that both the EOF and the correlation coefficient have a negative sign.) The change in globally averaged $\delta^{13}C_{DIC}$ is dominantly associated with changes in the $\delta^{13}C_{DIC}$ of AABW and AAIW. The Pacific EOF (average −0.035) has a greater magnitude than the Atlantic EOF (−0.026) so, volume effects aside, a global increase in $\delta^{13}C_{DIC}$ appears to be more pronounced in the Pacific Ocean, reflecting the additional influence of Antarctic water masses in this basin. Note that changes in global $\delta^{13}C_{DIC}$ are a result of surface restoring (as atmospheric concentrations are relaxed to observations), so that these changes would be expressed in the real Earth system as a change in atmospheric $\delta^{13}C$ of the opposite sign.

The second EOF does not exhibit a constant sign, but rather reflects a change in the spatial distribution of $\delta^{13}C_{DIC}$. In the Pacific, the EOF clearly reflects the variability in the exchange of $\delta^{13}C_{DIC}$ values between surface and deep water (i.e. via the export of particulate organic carbon POC). This interpretation also appears to be valid for the

5  Atlantic, especially given that these two fields are from a single EOF and so should reflect modes of variability that are closely related. The Atlantic EOF is complicated by the fact that changes in the surface $\delta^{13}C_{DIC}$ are transmitted to NADW, so that increased POC export results in elevated $\delta^{13}C_{DIC}$ in both surface waters and NADW. Whilst the basin-wide average of the second EOF in the Atlantic is of positive sign, in the Pacific it

10  is negative, suggesting that some of the light carbon exported from the surface waters of the Atlantic ends up in the deep Pacific. The second PC exhibits a correlation of −0.30 with global POC export, so as POC export increases the vertical gradient of $\delta^{13}C_{DIC}$ is reduced. This is discussed further in Sect. 6.2. Furthermore, the second PC exhibits a weak correlation (+0.2) with the globally-averaged DIC inventory, so that an

15  increase in the DIC reservoir is associated with an increase in the vertical gradient of $\delta^{13}C_{DIC}$, consistent with the application of this metric as a proxy for oceanic carbon storage and atmospheric $CO_2$ (Shackleton et al., 1983).

The third EOF takes generally positive values throughout the Atlantic and generally negative values throughout the Pacific, suggesting it describes a mechanism for inter-

20  basin exchange of $\delta^{13}C_{DIC}$. The greatest variability in the Atlantic is apparent at the boundary between Atlantic and Antarctic source waters, suggesting that this EOF reflects the relative influence of these water masses. Increased influence of NADW leads to increased values of deep Atlantic $\delta^{3}C_{DIC}$. This may be associated with a depletion of $^{13}C_{DIC}$ in the Arctic Ocean that possibly explains the lowered $\delta^{13}C_{DIC}$ in the surface

25  waters of the Northern Pacific (connected, in this model configuration, via diffusive transport through the shallow Bering Strait).

**Controls on the spatial distribution of oceanic $\delta^{13}C_{DIC}$**

P. B. Holden et al.

Back | Close

Full Screen / Esc

Printer-friendly Version

Interactive Discussion

## 6.2 Principal component emulation

In order to better understand which parameters, and hence which processes, are driving the spatial variability in simulated $\delta^{13}C_{DIC}$, simple linear emulators of the first three PCs corresponding to the EOFs described in Sect. 6.1 were derived.

$$\zeta(\theta) = a + \sum_{i=1}^{n} b_i \theta_i \tag{1}$$

where each PC $\zeta$ is expressed in terms of the 25 parameters $\theta_i$ and the scalar coefficients $a$ and $b_i$. Note that not all possible terms are included as the function is required to satisfy the Bayes Information Criterion. Linear terms were found sufficient to produce models with an adequate fit (model $R^2 \sim 85\%$ in each of the three PC models) and are more straightforward to interpret than more complex (e.g. quadratic) functions. Strong correlations exist between many parameter pairs; twelve parameter pairs exhibit a correlation (positive or negative) of $> 0.3$. These correlations were introduced by the ensemble design (which constrains for plausible pre-industrial states) and their presence makes cross-terms difficult to reliably interpret. The parameter coefficients $b_i$ for each of the PC emulators are plotted in Fig. 6.

In Sect. 6.1, the 1st EOF was identified as corresponding to changes in globally averaged $\delta^{13}C_{DIC}$. Parameters that are positively correlated with the global $\delta^{13}C_{DIC}$ (negatively correlated with the 1st PC) are wind-stress scaling (WSF, via surface layer mixing, leading to co-varying productivity and POC export), atmospheric heat diffusivity AHD (modulating the equator-pole temperature gradient), overall air-sea gas exchange strength (ASG) and ocean frictional drag (ODC). Increases in either the rain-ratio scalar (RRS) or the thermodynamic calcification rate power (TCP) act to decrease global $\delta^{13}C_{DIC}$ (increasing the export of $CaCO_3$ at the expense of POC export). Increases in OL0 act to warm the surface ocean by decreasing outgoing longwave radiation, decreasing global $\delta^{13}C_{DIC}$ via temperature fractionation during air-sea gas exchange. Note conversely that increases in AHD are associated with global cooling

Title Page

Abstract | Introduction

Conclusions | References

Tables | Figures

◄ | ►

◄ | ►

Back | Close

Full Screen / Esc

Printer-friendly Version

Interactive Discussion

and increased global $\delta^{13}C_{DIC}$. Ocean-mean $\delta^{13}C_{DIC}$ across the ensemble satisfies the relationship $\delta^{13}C_{DIC} = -0.091T + 2.159$ ($R^2 = 21\%$), where $T$ is the globally average sea-surface temperature, consistent with the temperature variation of oceanic $\delta^{13}C$ in thermodynamic equilibrium with atmospheric $\delta^{13}C$ of $CO_2$ of $-0.1\permil\,°C^{-1}$ (Mook, 1986).

The second PC appears to be mainly controlled by ocean diffusivities, wind stress scaling and by particulate export, remineralisation and air-sea gas exchange. This supports the inference that the second EOF describes the variability of exchange of carbon between the surface and deep ocean. The remineralisation depth (PRD) and the rain-ratio parameters (RRS and TCP) are all negatively correlated with export production. Increases in these parameters lead to the transfer of nutrients to deeper depths from where they cannot be re-mixed or upwelled as readily into the euphotic zone. This enhanced export of nutrients to depth thus decreases productivity so that an increase in these parameters results in increased near-surface values of $\delta^{13}C_{DIC}$.

The third PC clearly appears to be most strongly determined by isopycnal diffusivity OHD. This parameter correlates strongly with the strength of the AABW cell ($+0.37$), so that high values of OHD are associated with strengthened AABW circulation (within which DIC is depleted in $\delta^{13}C_{DIC}$ relative to NADW). Conversely, high values of APM, the other major determinant of the third PC, lead to strengthening of NADW (through a reduction in Atlantic surface salinity) and relative enrichment of $\delta^{13}C_{DIC}$ in the region where the boundaries between NADW and AABW are least clearly defined across the ensemble. As noted in Sect. 6.1, this effect appears to dominantly control the inter-basin contrast of $\delta^{13}C_{DIC}$, although the third PC is weakly correlated with the global average $\delta^{13}C$ ($+0.09$), suggesting it is also associated with an effect on the oceanic-mean of $\delta^{13}C_{DIC}$. Note that the three PCs together explain 99.4% of the variance in the ocean-mean $\delta^{13}C_{DIC}$, (86.0%, 12.5% and 0.9% respectively) so that almost all of the ensemble variability in ocean-mean pre-industrial $\delta^{13}C_{DIC}$ is described by these three modes of variability.

**Controls on the spatial distribution of oceanic $\delta^{13}C_{DIC}$**

P. B. Holden et al.

Title Page

Abstract | Introduction

Conclusions | References

Tables | Figures

◄ | ►|

◄ | ►

Back | Close

Full Screen / Esc

Printer-friendly Version

Interactive Discussion

# 7 Decomposition and emulation of the industrial $^{13}$C imprint

The method presented in Sect. 6 has been re-applied here to explore the change in the $\delta^{13}C_{DIC}$ distribution from pre-industrial to modern times. The EOF analysis and PC emulation is now applied to investigate the processes and parameters controlling the transient response to changes in the atmospheric carbon dioxide concentrations and its isotopic composition. We restrict our analysis to the first two EOFs, which describe 63 % and 18 % of the variance of the transient response, respectively. The Atlantic and Pacific EOFs, together with the parameters in the linear emulator (Eq. 1) are plotted in the upper two panels of Fig. 7.

The first EOF is of constant sign throughout both basins and so represents a change in global $\delta^{13}C_{DIC}$. This can be interpreted as simply due to the uptake of relatively light carbon from the atmosphere (in which the $^{13}$C-isotopic ratio has moved to lower values since pre-industrial times as a result of the burning of isotopically light fossil fuels). This change is restricted to depths up to $\sim 1000$ m in the Pacific, but the changes are redistributed to greater depth by NADW in the Atlantic. Unsurprisingly, the first PC emulator is dominated by the air-sea gas exchange parameter, which exhibits a correlation of $-0.89$ with the first PC. Globally increasing air-sea gas exchange strength acts to reduce the equilibration timescale of surface $\delta^{13}C_{DIC}$ with atmospheric $\delta^{13}$C. (The negative correlation is consistent with a lowering of the $\delta^{13}C_{DIC}$ as the EOF is of positive sign.) The equilibration timescale for $\delta^{13}C_{DIC}$ at the sea surface is of the order of a decade, hence there are large disequilibria at the air sea interface (see e.g. Gruber et al., 1999). In this regard, we note that the air-sea gas exchange parameterisation (following Wanninkhof, 1992) is proportional to the square of the wind speed, but is applied to the long-term average wind-speed, thus neglecting non-linear contributions of short-term variability which contribute substantially to the globally averaged air-sea gas transfer velocity (Wanninkhof, 1992). This introduces a systematic, spatially non-uniform bias in the disequilibrium of $\delta^{13}$C at the air-sea interface simulated by the model (typically underestimating the air-sea exchange at high latitudes).

Full Screen / Esc

Printer-friendly Version

Interactive Discussion

Further to this, a model error was recently discovered that introduces an artificial underestimation of the wind speed in some grid cells close to continental boundaries. The wide range over which the air-sea gas exchange was varied is likely to compensate for these shortcomings on the global scale. The ensemble-average of the global mean gas exchange coefficient for $CO_2$ of $0.038 +/- 0.14\,\mathrm{mol\,m^{-2}\,yr^{-1}\,\mu atm^{-1}}$ compares to the range of $(0.052 +/- 0.010)\,\mathrm{mol\,m^{-2}\,yr^{-1}\,\mu atm^{-1}}$, based on the estimate of the air-sea gas exchange velocity (and an estimate of the globally-averaged solubility of $CO_2$) by Naegler (2009). Thus, while the ASG parameter (0.1 to 0.5) spans the value for long-term average wind-speeds (0.39), given by Wanninkhof (1992), our central estimate for the global mean gas exchange coefficient is on the low side, which may reflect the information about fluctuating wind direction that is lost in calculating annually-averaged wind stress (from which wind speed is subsequently derived).

The second EOF describes the partitioning of $\delta^{13}C_{DIC}$ between surface and intermediate waters, indicative of the degree to which the isotopically-lightened surface carbon is mixed with intermediate waters. The linear emulator of the second PC is dominated by the global wind-stress scaling factor and the ocean drag coefficient. High values of either parameter increase mixing and upwelling, resulting in preferential lowering of $\delta^{13}C_{DIC}$ in intermediate waters relative to surface waters.

A similar analysis was performed for the anthropogenic change in DIC. The first EOF and the emulator coefficients for the change in DIC are plotted in Fig. 7. The dominant mode of DIC variability (54 % of the ensemble variance) is strikingly similar to the second EOF of the industrial change in $\delta^{13}C_{DIC}$. Furthermore, the corresponding PC emulators exhibit similar dependencies on model parameters, negatively correlated with the ocean drag (ODC) and wind-scaling (WSF), suggesting a close physical relationship between these modes of variability. The dominant mode of [13]C Suess-effect variability, arising from uncertainties in air-sea gas exchange, is largely absent from DIC variability, so that the processes controlling the distributions of industrial ^{13}C and $CO_2$ appear to be quite distinct.

# 8   Summary and conclusions

We have described the development and evaluation of a large ensemble of precalibrated parameterisations of GENIE for application to coupled carbon cycle problems. These parameterisations have already been applied to a range of experiments (Eby et al., 2012; Holden et al., 2012; Joos et al., 2012; Zickfeld et al., 2012). Work is presently in progress to apply them to a transient ensemble of simulations over the most recent glacial cycle, an experiment that has the potential to be constrained by a rich compilation of water-column $\delta^{13}C_{DIC}$ reconstructions from marine sediment data (e.g. Oliver et al., 2010).

We have applied singular vector decomposition and principal component emulation (Holden and Edwards, 2010) to investigate the modes of ensemble variability of the oceanic distribution of $\delta^{13}C_{DIC}$, considering both the pre-industrial state and the transient changes due to the Suess Effect. These analyses allow us to separate the natural and anthropogenic controls on the $\delta^{13}C_{DIC}$ distribution. The two analyses are connected by the possibility for compensating errors in the two distributions when modelling the modern ocean. For example, the second-order mode of variability in the preindustrial state (second EOF, Fig. 6) has a similar spatial distribution to the dominant mode of variability due to the Seuss effect (first EOF, Fig. 7), although they are controlled by quite distinct process (surface-deep ocean exchange and air-sea gas exchange, respectively).

The analysis provides a quantitative demonstration of the well-known balance between physical and biogeochemical processes that control the vertical gradient of $\delta^{13}C_{DIC}$ (Tagliabue and Bopp, 2008). These same controls exert an influence on the global DIC inventory in the equilibrium state (as distinct from change in the inventory due to anthropogenic forcing), supporting the use of the surface-deep gradient as a proxy for past ocean productivity-driven changes in atmospheric $CO_2$ (Shackleton et al., 1983).

Uncertainty in the distribution of $\delta^{13}C_{DIC}$ due to the Suess effect is dominated by air-sea gas exchange. The first EOF describes 63 % of the variability across the ensemble and is controlled almost entirely by the air-sea gas exchange parameter. The second EOF, describing 18 % of the variance, is driven by uncertainties in ocean parameters that control mixing of intermediate and surface waters. However, the decomposition of the distribution of anthropogenic DIC demonstrates, unsurprisingly, that air-sea gas exchange does not contribute substantially to uncertainty in the ocean carbon-sink. Rather, the dominant mode of variability (54 %) is strikingly similar to the second order variability in the Suess effect. Furthermore these two modes of variability are controlled by the same parameter relationships and hence, presumably, by the same physical processes. This comparison highlights well-known complications that arise when applying $\delta^{13}C_{DIC}$ as a constraint on the ocean sink and the need to separate the effects of uncertainty due to air-sea gas exchange. However, the similarity of the modes of variability of DIC and $\delta^{13}C_{DIC}$ after removal of the air-sea gas imprint strongly supports the value of observationally-based constraints imposed by $\delta^{13}C_{DIC}$ on DIC uptake (e.g. Quay et al., 2003). (Note these methodologies correct for the air-sea gas exchange signal). The need for a precise separation of the influence of air-sea gas exchange suggests that improved observational coverage of $\delta^{13}C_{DIC}$ is essential for improved quantification of the ocean-sink.

**Controls on the spatial distribution of oceanic $\delta^{13}C_{DIC}$**

P. B. Holden et al.

Title Page

Abstract | Introduction

Conclusions | References

Tables | Figures

⏮ | ⏭

◀ | ▶

Back | Close

Full Screen / Esc

Printer-friendly Version

Interactive Discussion

# References

Annan, J. D. and Hargreaves, J. C.: Efficient identification of ocean thermodynamics in a phys-ical/biogeochemical ocean model with an Iterative Importance Sampling Method, Ocean Model., 32, 205–215, doi:10.1016/j.ocemod.2010.02.003, 2010.

Antonov, J. I., Locarnini, R. A., Boyer, T. P., Mishonov, A. V., and Garcia, H. E.: World Ocean At-las 2005, Volume 2, edited by: Salinity. S., Levitus, NOAA Atlas NESDIS 62, US Government Printing Office, Washington, D.C., 182 pp., 2006.

Archer, D.: A data-driven model of the global calcite lysocline, Global Biogeochem. Cy., 10, 511–526, doi:10.1029/96GB01521, 1996.

Bondeau, A., Smith, P. C., Zaehle, S., Schaphoff, S., Lucht, W., Cramer, W., Gerten, D., Lotze-Campen, H., Müller, C., Reichstein, M., and Smith, B.: Modelling the role of agriculture for the 20th century global terrestrial carbon balance, Glob. Change Biol., 13, 679–706, doi:doi:10.1111/j.1365-2486.2006.01305.x, 2007.

Bouttes, N., Paillard, D., and Roche, D. M.: Impact of brine-induced stratification on the glacial carbon cycle, Clim. Past, 6, 575–589, doi:10.5194/cp-6-575-2010, 2010.

Bouttes, N., Paillard, D., Roche, D. M., Brovkin, V., and Bopp L.: Last Glacial Maximum $CO_2$ and $\delta^{13}$C successfully reconciled, Geophys. Res. Lett., 38, L02705, doi:10.1029/2010GL044499, 2011.

Cavalieri, D. J., Parkinson, C. L., and Yinnikov, K. Y.: 30-year satellite record reveals con-trasting Arctic and Antarctic decadal sea-ice variability, Geophys. Res. Lett., 30, 1970, doi:10.1029/2003GL018031, 2003.

Chikamoto, M. O., Abe-Ouchi, A., Oka, A., Ohgaito, R., and Timmermann, A.: Quantifying the ocean's role in glacial $CO_2$ reductions, Clim. Past, 8, 545–563, doi:10.5194/cp-8-545-2012, 2012.

Colbourn, G.: Weathering effects on the carbon cycle in an Earth System Model, PhD thesis, School of Environmental Sciences, University of East Anglia, http://ethos.bl.uk/OrderDetails.do?uin=uk.bl.ethos.537151, 2011.

Conkright, M. E., Locarnini, R. A., Garcia, H. E., OBrien, T. D., Boyer, T. P., Stephens, C., and Antonov, J. I.: World Ocean Atlas 2001: Objective Analysis, Data, Statistics and Figures, CD-ROM Documentation, National Oceanographic Data Center, Silver Spring, MD, 2002.

Title Page

| Abstract | Introduction |
| Conclusions | References |
| Tables | Figures |

◀◀ ▶▶

◀ ▶

Back Close

Full Screen / Esc

Printer-friendly Version

Interactive Discussion

Doney, S. C., Lindsay, K., Fung, I., and John, J.: Natural variability in a stable, 100-yr global coupled climate-carbon cycle simulation, J. Climate, 19, 3033–3054, doi:10.1175/JCLI3783.1, 2006.

Eby, M., Weaver, A. J., Alexander, K., Zickfeld, K., Abe-Ouchi, A., Cimatoribus, A. A., Crespin, E., Drijfhout, S. S., Edwards, N. R., Eliseev, A. V., Feulner, G., Fichefet, T., Forest, C. E., Goosse, H., Holden, P. B., Joos, F., Kawamiya, M., Kicklighter, D., Kienert, H., Matsumoto, K., Mokhov, I. I., Monier, E., Olsen, S. M., Pedersen, J. O. P., Perrette, M., Philippon-Berthier, G., Ridgwell, A., Schlosser, A., Schneider von Deimling, T., Shaffer, G., Smith, R., Spahni, R., Sokolov, A. P., Steinacher, M., Tachiiri, K., Tokos, K., Yoshimori, M., Zeng, N. and Zhao, F.: Historical and idealized climate model experiments: and EMIC intercomparison, Clim. Past Discuss., 8, 4121–4181, doi:doi:10.5194/cpd-8-4121-2012, 2012.

Edwards, N. R. and Marsh, R.: Uncertainties due to transport-parameter sensitivity in an efficient 3-D ocean-climate model, Clim. Dynam., 24, 415–433, doi:10.1007/s00382-004-0508-8, 2005.

Edwards, N. R., Cameron, D., and Rougier, J.: Precalibrating an intermediate complexity climate model, Clim. Dynam., 37, 1469–1482, doi:10.1007/s00382-010-0921-0, 2011.

Friedlingstein, P., Cox, P., Betts, R., Bopp, L., von Bloh, W., Brovkin, V., Cadule, P., Doney, S., Eby, M., Fung, I., Bala, G., John, J., Jones, C., Joos, F., Kato, F., Kawamiya, M., Knorr, W., Lindsay, K., Matthews, H. D., Raddatz, T., Rayner, P., Reick, C., Roeckner, E., Schnitzler, K. G., Schnur, R., Strassman, K., Weaver Yoshikawa, A. J., C., and Zeng, N.: Climate-carbon cycle feedback analysis: results from the $C^4$MIP model intercomparison, J. Climate, 19, 3337–3353, doi:10.1175/JCLI3800.1, 2006.

Garcia, H. E., Locarnini, R. A., Boyer, T. P., and Antonov, J. I.: World Ocean Atlas 2005, Volume 4: Nutrients (phosphate, nitrate, silicate), edited by: Levitus, S., NOAA Atlas NESDIS 64, US Government Printing Office, Washington, D.C., 396 pp., 2006.

Gruber, N., Keeling, C. D., Bacastow, R. B., Guenther, P. R., Lueker, T. J., Wahlen, M., Meijer, H. A., Mook, W. G., and Stocker, T. F.: Spatiotemporal patterns of carbon-13 in the global surface oceans and the oceanic Suess effect, Global Biogeochem. Cy., 13, 307–335, doi:10.1029/1999GB900019, 1999.

Holden, P. B. and Edwards, N. R.: Dimensionally reduced emulation of an AOGCM for application to integrated assessment modelling, Geophys. Res. Lett., 37, L21707 doi:10.1029/2010GL045137, 2010.

Holden, P. B., Edwards, N. R., Oliver, K. I. C., Lenton, T. M., and Wilkinson, R. D.: A probabilistic calibration of climate sensitivity and terrestrial carbon change in GENIE-1, Clim. Dynam., 35, 785–806, doi:10.1007/s00382-009-0630-8, 2010.

Holden, P. B., Edwards, N. R., Gerten, D., and Schaphoff, S.: A model-based constraint of $CO_2$ fertilisation, Biogeosciences Discuss., 9, 9425–9451, doi:10.5194/bgd-9-9425-2012, 2012.

Jones, P. D., New, M., Parker, D. E., Martin, S., and Rigor, I. G.: Surface air temperature and its changes over the past 150 years, Rev. Geophys., 37, 173–199, doi:10.1029/1999RG900002, 1999.

Joos, F. and Bruno, M.: Long-term variability of the terrestrial and oceanic carbon sinks and the budgets of the carbon isotopes $^{13}$C and $^{14}$C, Global Biogeochem. Cy., 12, 277–295, doi:10.1029/98GB00746, 1998.

Joos, F., Roth, R., Fuglestvedt, J. S., Peters, G. P., Enting, I. G., von Bloh, W., Brovkin, V., Burke, E. J., Eby, M., Edwards, N. R., Friedrich, T., Frölicher, T. L., Halloran, P. R., Holden, P. B., Jones, C., Kleinen, T., Mackenzie, F., Matsumoto, K., Meinshausen, M., Plattner, G.-K., Reisinger, A., Segschneider, J., Shaffer, G., Steinacher, M., Strassmann, K., Tanaka, K., Timmermann, A., and Weaver, A. J.: Carbon dioxide and climate impulse response functions for the computation of greenhouse gas metrics: a multi-model analysis, Atmos. Chem. Phys. Discuss., 12, 19799–19869, doi:10.5194/acpd-12-19799-2012, 2012.

Kanzow, T., Cunningham, S. A., Johns, W. E., Hirschi, J. J. M., Chidichimo, M. P., Atkinson, C., Beal, L. M., Bryden, H. L., and Collins, J.: Seasonal variability of the Atlantic meridional overturning circulation at 26.58° N, J. Climate, 23, 5678–5698, 2010.

Keeling, C. D.: The Suess Effect: $^{13}$Carbon and $^{14}$Carbon interactions, Environ. Int., 2, 229–300, doi:10.1016/0160-4120(79)90005-9, 1979.

Keeling, R. F., Piper, S. C., Bollenbacher, A. F. and Walker., S. J.: Monthly atmospheric $^{13}$C/$^{12}$C isotopic ratios for 11 SIO stations. In Trends: A Compendium of Data on Global Change. Carbon Dioxide Information Analysis Center, Oak Ridge National Laboratory, US Department of Energy, Oak Ridge, Tenn., USA, 2010.

Kohfeld, K. E. and Ridgwell, A.: Glacial-interglacial variability in atmospheric $pCO_2$, in Surface Ocean-Lower Atmosphere Processes, Geophys. Monogr. Series, 187, 251–286, doi:10.1029/2008GM000845, 2009.

Kroopnick, P. M.: The distribution of $^{13}$C of $\Sigma CO_2$ in the world oceans, Deep-Sea Res., 32, 57–84, doi:10.1016/0198-0149(85)90017-2, 1985.

**Controls on the spatial distribution of oceanic $\delta^{13}C_{DIC}$**

P. B. Holden et al.

Lenton, T. M., Williamson, M. S., Edwards, N. R., Marsh, R., Price, A. R., Ridgwell, A. J., Shepherd, J. G., Cox, S. J., and the GENIE team: Millennial timescale carbon cycle and climate change in an efficient Earth system model, Clim. Dynam., 26, 687–711, doi:10.1007/s00382-006-0109-9, 2006.

Le Quéré, C., Rödenbeck, C., Buitenhuis, E. T., Conway, T. J., Langenfelds, R., Gomez, A., Labuschagne, C., Ramonet, M., Nakazawa, T., Metzl, N., Gillett, N., and Heimann, M.: Saturation of the Southern Ocean sink due to recent climate change, Nature, 316, 1735–1738, doi:10.1126/science.1136188, 2007.

Locarnini, R. A., Mishonov, A. V., Antonov, J. I., Boyer, T. P., and Garcia, H. E.: World Ocean Atlas 2005, Volume 1: Temperature, edited by: Levitus, S., NOAA Atlas NESDIS 61, US Government Printing Office, Washington, D.C., 182 pp., 2006.

Lüthi, D., Le Floch, M., Bereiter, B., Blunier, T., Barnol Siegenthaler, J. M., U., Raynaud, D., Jouzel, J., Fischer, H., Kawamura, K., and Stocker, T. F.: High-resolution carbon-dioxide concentration record 650 000–800 000 years before present, Nature, 453, 379–382, doi:10.1038/nature06949, 2008.

Mahowald, N., Baker, A., Bergametti, G., Brooks, N., Duce, R., Jickells, T., Kubilay, N., Prospero, J., and Tegen, I.: The atmospheric global dust cycle and iron inputs to the ocean, Global Biogeochem. Cy., 19, GB4025, doi:10.1029/2004GB002402, 2005.

Marsh, R., Müller, S. A., Yool, A., and Edwards, N. R.: Incorporation of the C-GOLDSTEIN efficient climate model into the GENIE framework: "eb_go_gs" configurations of GENIE, Geosci. Model Dev., 4, 957–992, doi:10.5194/gmd-4-957-2011, 2011.

Mook, W. G.: $^{13}$C in atmospheric $CO_2$, Neth. J. Sea Res., 20, 211–223, doi:10.1016/0077-7579(86)90043-8, 1986.

Müller, S. A., Joos, F., Edwards, N. R., and Stocker, T. F.: Water mass distribution and ventilation time scales in a cost-efficient, 3-dimensional ocean model, J. Climate, 19, 5479–5499, doi:10.1175/JCLI3911.1, 2006.

Naegler, T.: Reconciliation of excess $^{14}$C-constrained global $CO_2$ piston velocity estimates, Tellus B, 61, 372–384, doi:10.1111/j.1600-0889.2008.00408.x, 2009.

Omta, A. W., Bruggeman, J., Kooljman, S. A. L. M., and Dijkstra, H. A.: Biological carbon pump revisited: feedback mechanisms between climate and the Redfield ratio, Geophys. Res. Lett., 33, L14613, doi:10.1029/2006GL026213, 2006.

Title Page

Abstract | Introduction

Conclusions | References

Tables | Figures

◀ | ▶

◀ | ▶

Back | Close

Full Screen / Esc

Printer-friendly Version

Interactive Discussion

Oliver, K. I. C. and Edwards, N. R.: Location of potential energy sources and the export of dense water from the Atlantic Ocean, Geophys. Res. Lett., 35, L22604, doi:10.1029/2008GL035537, 2008.

Oliver, K. I. C., Hoogakker, B. A. A., Crowhurst, S., Henderson, G. M., Rickaby, R. E. M., Edwards, N. R., and Elderfield, H.: A synthesis of marine sediment core $\delta^{13}$C data over the last 150 000 years, Clim. Past, 6, 645–673, doi:10.5194/cp-6-645-2010, 2010.

Quay, P., Sonnerup, R., Westby, T., Stutsman, J., and McNichol, A.: Changes in the $^{13}$C/$^{12}$C of dissolved inorganic carbon in the ocean as a tracer of anthropogenic $CO_2$ uptake, Global Biogeochem. Cy., 17, 1004, doi:10.1029/2001GB001817, 2003.

Ridgwell, A. and Hargreaves, J. C.: Regulation of atmospheric $CO_2$ by deep-sea sediments in an Earth system model, Global Biogeochem. Cy., 21, GB2008, doi:10.1029/2006GB002764, 2007.

Ridgwell, A., Hargreaves, J. C., Edwards, N. R., Annan, J. D., Lenton, T. M., Marsh, R., Yool, A., and Watson, A.: Marine geochemical data assimilation in an efficient Earth System Model of global biogeochemical cycling, Biogeosciences, 4, 87–104, doi:10.5194/bg-4-87-2007, 2007a.

Ridgwell, A., Zondervan, I., Hargreaves, J. C., Bijma, J., and Lenton, T. M.: Assessing the potential long-term increase of oceanic fossil fuel $CO_2$ uptake due to $CO_2$-calcification feedback, Biogeosciences, 4, 481–492, doi:10.5194/bg-4-481-2007, 2007b.

Ritz, S. P., Stocker, T. F., and Joos, F.: A coupled dynamical ocean-energy balance atmosphere model for paleoclimate studies, J. Climate, 24, 349–375, doi:10.1175/2010JCLI3351.1, 2011.

Saltelli, A., Chan, K., and Scott, M.: Sensitivity Analysis, Wiley, New York, 2000.

Shackleton, N. J., Hall, M. A., Line, J., and Shuxi, C.: Carbon isotope data in core V19-30 confirm reduced carbon dioxide concentration in the ice age atmosphere, Nature, 306, 319–322, doi:10.1038/306319a0, 1983.

Stephens, B. B. and Keeling, R. F.: The influence of Antarctic sea ice on glacial-interglacial $CO_2$ variations, Nature, 404, 171–174, doi:10.1038/35004556, 2000.

Tagliabue, A. and Bopp, L.: Towards understanding global variability in ocean carbon-13, Global Biogeochem. Cy., 22, GB1025, doi:10.1029/2007GB003037, 2008.

Wanninkhof, R.: Relationship between wind speed and gas exchange over the ocean, J. Geophys. Res., 97, 7373–7382, doi:10.1029/92JC00188, 1992.

Watson, A. J., Bakker, D. C. E., Ridgwell, A. J., Boyd, P. W., and Law, C. S.: Effect of iron supply on Southern Ocean $CO_2$ uptake and implications for glacial atmospheric $CO_2$, Nature, 407, 730–733, doi:10.1038/35037561, 2000.

Williamson, M. S., Lenton, T. M., Shepherd, J. G., and Edwards, N. R.: An efficient numerical terrestrial scheme (ENTS) for Earth system modelling, Ecol. Model., 198, 362–374, doi:10.1016/j.ecolmodel.2006.05.027, 2006.

Zickfeld, K., Eby, M., Weaver, A. J., Crespin, E., Fichefet, T., Goosse, H., Philippon-Berthier, G., Edwards, N. R., Holden, P. B., Eliseev, A., Mokhov, I., Feulner, G., Kienert, H., Perrette, M., Schneider von Deimling, T., Forest, C. E., Joos, F., Spahni, R., Steinacher, M., Kawamiya, M., Tachiiri, K., Kicklighter, D., Monier, E., Schlosser, A., Sokolov, A., Matsumoto, K., Tokos, K., Olsen, S. M., Pedersen, J. O. P., Shaffer, G., Ridgwell, A., Zeng, N., and Zhao, F.: Long-term climate change commitment and reversibility: an EMIC intercomparison, J. Climate, submitted, 2012.

Title Page

Abstract | Introduction

Conclusions | References

Tables | Figures

◄ | ►

◄ | ►

Back | Close

Full Screen / Esc

Printer-friendly Version

Interactive Discussion

P. B. Holden et al.

**Table 1.** Varied model parameters of the simulation ensemble.

| Module | Code | Parameter name | Parameter description | Min. | Max. | Dist. |
|---|---|---|---|---|---|---|
| EMBM | AHD | diffamp(1) | Atmospheric heat diffusivity ($m^2 s^{-1}$) | 1.0e6 | 4.5e6 | LOG |
| | AMD | diffamp(2) | Atmospheric moisture diffusivity ($m^2 s^{-1}$) | 5.0e4 | 3.22e6 | LOG |
| | APM | scl_fwf | Atlantic-Pacific moisture flux scaling | 0.1 | 2.0 | LIN |
| | OL0 | olr_adj0 | Clear skies OLR reduction ($Wm^{-2}$) | 2.46 | 10.0 | LIN |
| GOLDSTEIN | OHD | diff(1) | Isopycnal diffusivity ($m^2 s^{-1}$) | 300 | 9000 | LOG |
| | OVD | diff(2) | Reference diapycnal diffusivity ($m^2 s^{-1}$) | 2.0e-5 | 2.0e-4 | LOG |
| | OP1 | ediffpow1 | Power law for diapycnal diffusivity depth profile | 0.0 | 1.5 | LIN |
| | ODC | adrag | Ocean inverse drag coefficient (days) | 0.5 | 5.0 | LIN |
| | WSF | scf | Wind-scale factor | 1.0 | 3.0 | LIN |
| SEAICE | SID | diffsic | Sea-ice diffusivity ($m^2 s^{-1}$) | 5.0e3 | 1.0e5 | LOG |
| ENTS | VFC | k17 | Fractional vegetation dependence on veg carbon density ($m^2$ kgC) | 0.38 | 1.0 | LIN |
| | VBP | k18 | Base rate of photosynthesis (kgC $m^{-2}$ yr) | 3.0 | 5.5 | LIN |
| | VRA | k20 | Vegetation respiration activation energy (J $mol^{-1}$) | 24 000 | 72 000 | LIN |
| | LLR | k26 | Leaf litter rate ($yr^{-1}$) | 0.075 | 0.26 | LIN |
| | SRT | k32 | Soil respiration temperature dependence (K) | 197 | 241 | LIN |
| BIOGEM | PMX | | Dummy parameter (Sect. 3.1) | 5e-7 | 5e-6 | LOG |
| | PHS | par_bio_c0_PO4 | $PO_4$ half-saturation concentration (mol $kg^{-1}$) | 5e-8 | 1e-6 | LOG |
| | PRP | par_bio_remin_POC_frac2 | Initial proportion of POC export as recalcitrant fraction | 0.01 | 0.1 | LIN |
| | PRD | par_bio_remin_POC_eL1 | e-folding remineralisation depth of non-recalcitrant POC (m) | 100 | 1000 | LIN |
| | RRS | par_bio_red_POC_CaCO3 | Rain ratio scalar | 0.02 | 0.1 | LIN |
| | TCP | par_bio_red_POC_CaCO3_pP | Thermodynamic calcification rate power | 0.2 | 2.0 | LIN |
| | PRC | par_bio_remin_CaCO3_frac2 | Initial proportion of $CaCO_3$ export as recalcitrant fraction | 0.1 | 1.0 | LIN |
| | CRD | par_bio_remin_CaCO3_eL1 | e-folding remineralisation depth of non-recalcitrant $CaCO_3$ (m) | 300 | 3000 | LIN |
| | FES | par_det_Fe_sol | Iron solubility | 0.001 | 0.1 | LOG |
| | ASG | par_gas_transfer_a | Air-sea gas exchange parameter | 0.1 | 0.5 | LIN |

**Table 2.** The eight plausibility metrics. ABC test: the "Approximate Bayesian Calibration" ranges accepted as potentially plausible when a parameter set was applied to the emulators. All eight tests passed for each of the 1000 parameter sets which were applied to the simulator. Plausibility test: the range accepted for a simulation for it to be classified as plausible. All eight tests are passed by the 471 simulations accepted in the EFPC ensemble. Ensemble mean and ensemble range describe the characteristics of the EFPC ensemble.

| | Observations | ABC test | Plausibility test | Ensemble mean | Ensemble range |
|---|---|---|---|---|---|
| SAT: global surface air temperature (°C) | ~14 Jones et al. (1999) | 12 to 16 | 11 to 17 | 13.6 ± 1.1 | 11.7 to 16.2 |
| MINA: minimum Atlantic stream Function (Sv) | ~ −4 Kanzow et al. (2010) | −6 to −3 | −8 to −1 | −4.1 ± 1.0 | −6.8 to −1.0 |
| MAXA: maximum Atlantic stream function (Sv) | ~19 Kanzow et al. (2010) | 12 to 22 | 10 to 30 | 17.5 ± 3.2 | 10.0 to 25.8 |
| SHSI: 31/12 Antarctic sea-ice area (million km$^2$) | ~7 Cavalieri et al. (2003) | 5 to 15 | 1 to 13 | 6.8 ± 2.8 | 1.2 to 12.9 |
| CVEG: global vegetative carbon (GTC) | 450 to 650 Bondeau et al. (2007) | 350 to 700 | 300 to 800 | 492 ± 94 | 326 to 762 |
| CSOIL: global soil carbon (GTC) | 850 to 2400 Bondeau et al. (2007) | 1000 to 2200 | 750 to 2500 | 1351 ± 308 | 896 to 2430 |
| CACO3: Weight percentage CaCO$_3$ | ~35 Archer (1996) | 30 to 40 | 20 to 50 | 34.1 ± 7.8 | 20.0 to 50.0 |
| O2: global average dissolved oxygen (µmol kg$^{-1}$) | ~170 Konkright et al. (2002) | 137 to 197 | 117 to 217 | 165 ± 20 | 117 to 216 |
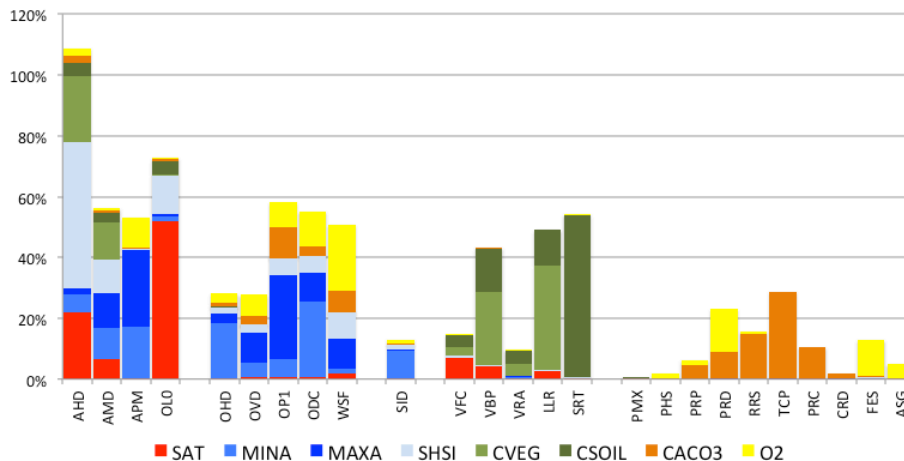
**Fig. 1.** Total effects for the eight plausibility emulators, normalised to total 100 %. The colours identifiy the eight emulators. Parameters are grouped along the horizontal axis according to Earth-system module (atmosphere, ocean, sea ice, land vegetation and ocean biogeochemistry).
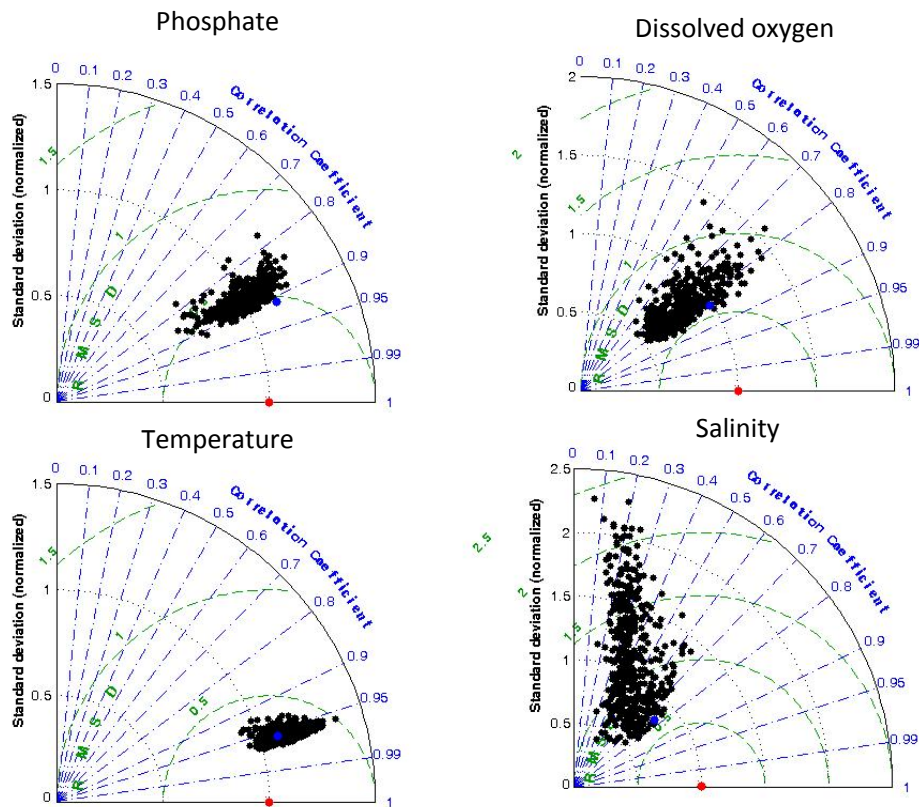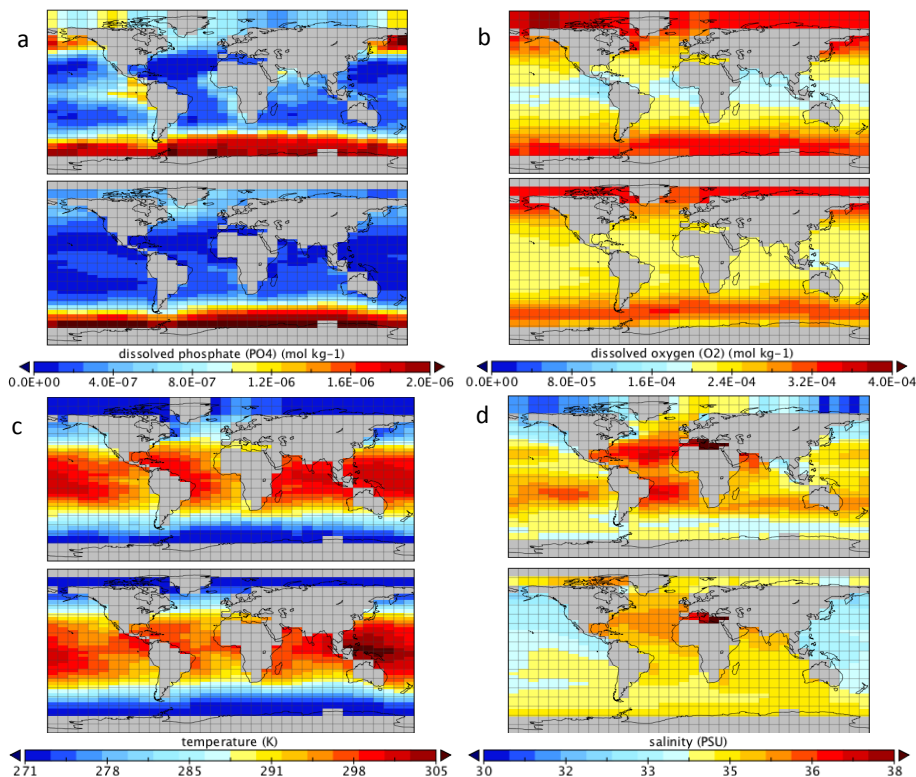
**Fig. 2.** Taylor diagrams for the EFPC ensemble (dissolved phosphate, dissolved oxygen, temperature and salinity). Black circles are the 471 ensemble members. Blue circles are the outputs of an optimised model configuration (Ridgwell and Death, 2012).

Title Page

Abstract | Introduction

Conclusions | References

Tables | Figures

|◄ | ►|

◄ | ►

Back | Close

Full Screen / Esc

Printer-friendly Version

Interactive Discussion

**Fig. 3.** Surface observations (upper panels, gridded onto the model grid as in Ridgwell et al., 2007a, here for the higher vertical resolution of the applied model) compared to EPFC ensemble averages (lower panels) for **(a)** dissolved phosphate (Garcia et al., 2006), **(b)** dissolved oxygen (Garcia et al., 2006), **(c)** temperature (Locarnini et al., 2006) and **(d)** salinity (Antonov et al., 2006).

**Fig. 4.** Atlantic cross-sections (25°,W). Observations (upper panels, gridded on to the model grid as in Ridgwell et al., 2007a, here for the higher vertical resolution of the applied model) compared to EPFC ensemble averages (lower panels) for **(a)** dissolved phosphate (Garcia et al., 2006), **(b)** dissolved oxygen (Garcia et al., 2006), **(c)** temperature (Locarnini et al., 2006) and **(d)** salinity (Antonov et al., 2006).

Full Screen / Esc

Printer-friendly Version

Interactive Discussion
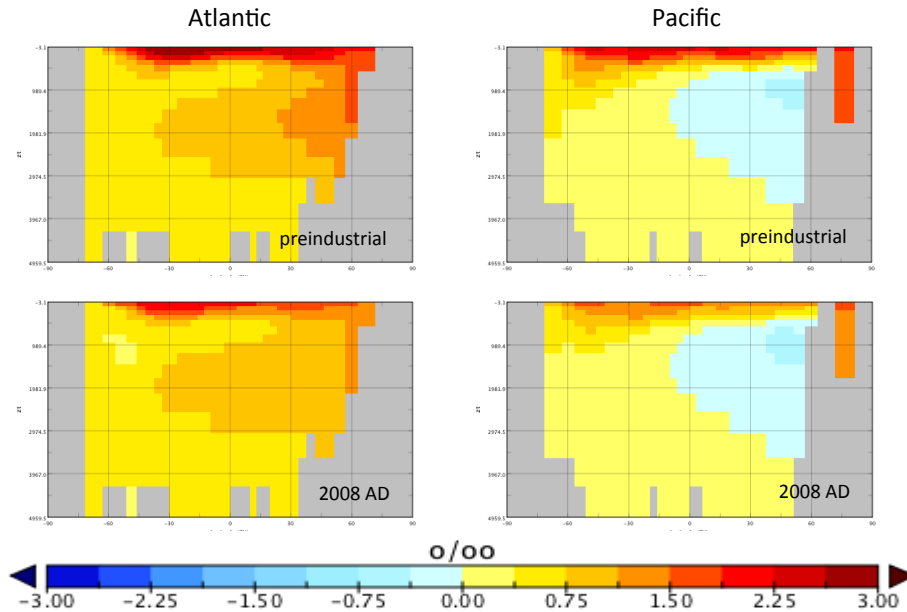
**Fig. 5.** Ensemble averaged $\delta^{13}C_{DIC}$ transects through the Atlantic (25° W) and Pacific (155° W) from the preindustrial spun-up states (upper panels) and at the end of the 1858 to 2008 AD transient simulations (lower panels).
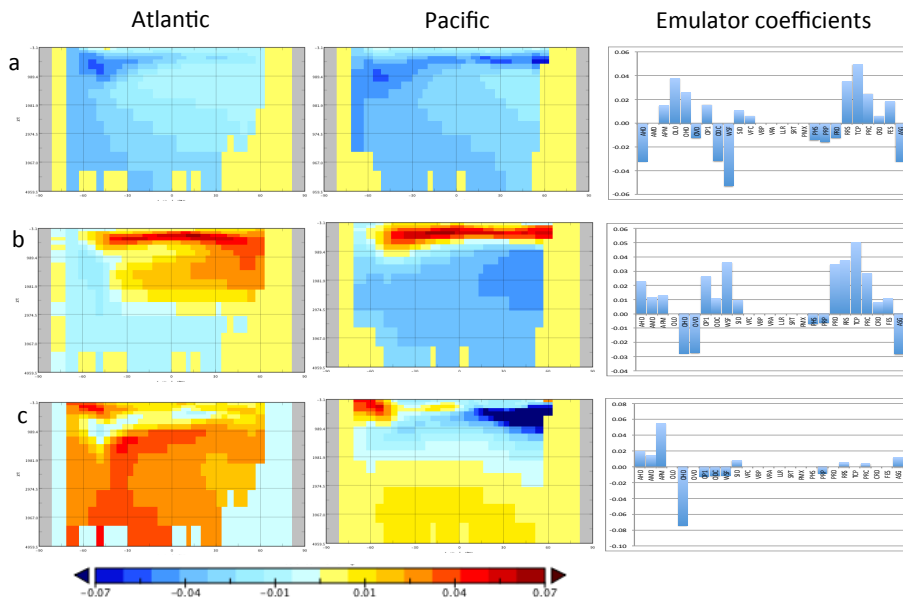
**Fig. 6.** Preindustrial EOFs and PC emulator coefficients. **(a)** First EOF (42 % of ensemble variance) **(b)** second EOF (27 % of ensemble variance) and **(c)** third EOF (11 % of ensemble variance).
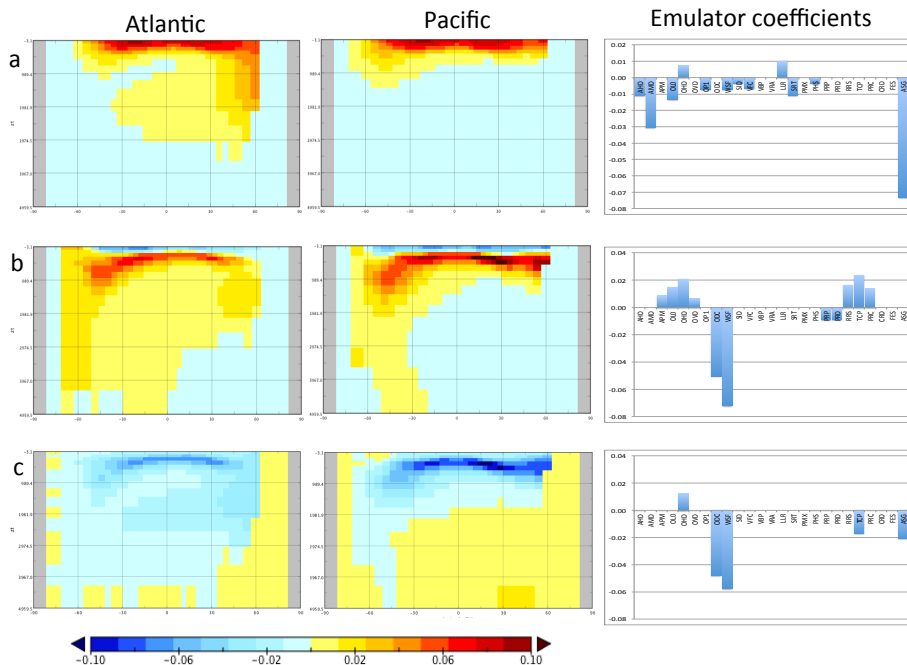
**Fig. 7.** EOFs and PC emulator coefficients for anthropogenically-forced change (1858 to 2008 AD). **(a)** First EOF of $\delta^{13}C_{DIC}$ change (63 % of ensemble variance) **(b)** second EOF of $\delta^{13}C_{DIC}$ change (18 % of ensemble variance) and **(c)** first EOF of DIC change (54 % of ensemble variance).